

Banner appropriate to article type will appear here in typeset article

1 Transition to turbulence in wind-drift layers

2 **Gregory LeClaire Wagner,^a† Nick Pizzo,^{b,c} Luc Lenain,^c Fabrice Veron^d**

3 ^aMassachusetts Institute of Technology

4 ^bUniversity of Rhode Island Graduate School of Oceanography

5 ^cScripps Institution of Oceanography, University of California, San Diego

6 ^dUniversity of Delaware

7 (Received xx; revised xx; accepted xx)

8 A light breeze rising over calm water initiates an intricate chain of events that culminates in
9 a centimeters-deep turbulent shear layer capped by gravity-capillary ripples. At first, viscous
10 stress accelerates a laminar wind-drift layer until small surface ripples appear. Then a second
11 “wave-catalyzed” instability grows in the wind-drift layer, before sharpening into along-
12 wind jets and downwelling plumes, and finally devolving into three-dimensional turbulence.
13 This paper elucidates the evolution of wind-drift layers after ripple inception using wave-
14 averaged numerical simulations with a random initial condition and a constant-amplitude
15 representation of the incipient surface ripples. Our model reproduces qualitative aspects of
16 laboratory measurements similar those reported by Veron & Melville (2001), validating the
17 wave-averaged approach. But we also find that our results are disturbingly sensitive to the
18 amplitude of the prescribed surface wave field, raising the question whether wave-averaged
19 models are truly “predictive” if they do not also describe the coupled evolution of the surface
20 waves together with the flow beneath.

21 1. Introduction

22 The appearance of surface ripples beneath gusts of wind is an everyday experience on the
23 water, belying a surprisingly intricate chain of events unfolding beneath the surface. There, an
24 accelerating wind-drift layer breeds two instabilities in sequence: first the surface instability
25 that generates ripples, followed by a subsurface instability whose growth, finite amplitude
26 saturation, and destabilization to three-dimensional perturbations ultimately gives way to
27 persistent turbulence in the centimeters-thick wind-drift layer.

28 This ubiquitous transition-to-turbulence scenario was observed in a series of laboratory
29 experiments reported by Melville *et al.* (1998), Veron & Melville (1999) and Veron &
30 Melville (2001) that subjected an initially quiescent wave tank to a turbulent airflow rapidly
31 accelerated from rest to a constant airspeed. One of Veron & Melville (2001)’s key results
32 is that both the generation of surface ripples and the transition to turbulence are suppressed
33 by surfactant layered on the water surface. The surfactant experiment proves that ripples are
34 intrinsic to the second slow instability implicated in the turbulent transition of the wind-drift
35 layer under typical conditions (disproving Handler *et al.* (2001)’s hypothesis, repeated by
36 Thorpe (2004), that the transition to turbulence is convective.)

† Gregory Wagner, gregory.leclaire.wagner@gmail.com

Motivated by Veron & Melville (2001)'s experimental results, we propose a wave-averaged model based on the "Craik-Leibovich" (CL) Navier-Stokes equations (Craik & Leibovich 1976) for the development of wind-drift layers — eventually leading to a transition to turbulence — after the appearance of capillary ripples. We focus narrowly on a comparison with a new laboratory experiment similar to those reported by Veron & Melville (2001) and described in section 2. The predictions of our wave-averaged model are developed in section 3. We mix analytical results from Veron & Melville (2001) on the initial laminar developments with a linear instability analysis of the wind-drift layer just after ripple inception, and with numerical simulations of nonlinear development of the second slow instability from ripple inception to fully developed wind-drift turbulence.

We have two goals: first, we seek a more detailed understanding of the wind-drifted transition to turbulence. Second, we seek to validate the wave-averaged Craik-Leibovich (CL) momentum equation, which is central to parameterization of ocean surface boundary layer turbulence (see for example D'Asaro *et al.* (2014); Harcourt (2015); Reichl & Li (2019)). Toward this second goal we make some progress and find that our CL-based model qualitatively replicates the laboratory measurements — most strikingly during the transition to turbulence depicted in figure 4. Yet we also find our results are delicately sensitive to the parameters of the prescribed ripples, which owing to uncertainty about the evolving, two-dimensional state of the ripples surrounding the transition to the turbulence, prevents unambiguous conclusions about CL validity. In section 4, we argue that this sensitivity implies that CL is "incomplete" because it does not also predict the *response* of the wave field to the currents and turbulence beneath.

2. Laboratory experiments of winds rising over calm water

This paper uses an experiment similar to those reported by Melville *et al.* (1998) and Veron & Melville (2001). The experiment was conducted in the 42-m long, 1-m wide, 1.25-m high wind-wave-current tank at the Air-Sea Interaction Laboratory of the University of Delaware, and used a computer-controlled recirculating wind tunnel to accelerate a turbulent airflow to 10 m s^{-1} over 65 s. The water depth was maintained at 0.71 m and observations were collected at a fetch of 12 m. An artificial wave-absorbing beach dissipated wave energy and eliminate wave reflections at the downwind end of the tank.

2.1. Laser-induced fluorescence (LIF) observations

The evolution of initially-surface-concentrated dye was observed with a Laser-Induced Fluorescence (LIF) system. Images were acquired with a CCD camera (Jai TM4200CL, 2048×2048 pixels) equipped with an 85 mm Canon EF lens focused at the air-water interface. Illumination was provided by a thin 3 mm thick laser light sheet generated by a pulsed dual-head Nd-Yag laser (New Wave Research, 120 mJ/pulse, 3–5 ns pulse duration). The laser light illuminated a thin layer of fluorescent dye carefully applied to the water surface prior to each experiment. Observations were conducted with the light sheet in both along-wind and transverse directions. The LIF camera collected images at a 7.2Hz frame rate and with a field of view of 11.6×11.6 cm in the along-wind configuration, and 13.9×13.9 cm in the transverse direction. An edge detection algorithm based on local variations of image intensity gradients, computed by kernel convolution was used to identify the location of the surface in the LIF images (Buckley & Veron 2017).

2.2. Thermal Marking Velocimetry (TMV)

In addition to LIF, we employed Thermal Marking Velocimetry (TMV), as developed by Veron & Melville (2001) and Veron *et al.* (2008), to measure the surface velocity by tracking

83 laser-generated Lagrangian heat markers in thermal imagery of water surfaces. In the present
 84 experiment, infrared images of the surface were captured by a 14-bit, 640×512 quantum
 85 well infrared photodetector (QWIP — 8.0–9.2 μm) FLIR SC6000 infrared camera operated
 86 at a 43.2 Hz frame rate, with an integration time of 10 ms, and a stated rms noise level below
 87 35 mK. After image correction to account for the slightly off-vertical viewing angle of the
 88 imager, the resulting image sizes were 24.6×24.6 cm.

89 The infrared imager is sensitive enough to detect minute, turbulent temperature variations
 90 in the surface thermal skin layer (Jessup *et al.* 1997; Zappa *et al.* 2001; Veron & Melville
 91 2001; Sutherland & Melville 2013). It thus easily detects active weakly-heated markers,
 92 generated by a 60 W air-cooled CO₂ laser (Synrad Firestar T60) equipped with an industrial
 93 marking head (Synrad FH Index) and two servo-controlled scanning mirrors programmed to
 94 lay down a pattern of 16 spots with 0.8 cm diameter and at a frequency of 1.8 Hz.

95 The spatially averaged surface velocity was estimated by tracking the geometric centroid
 96 of these Lagrangian heat markers for approximately one second. Both Gaussian interpolation
 97 (which has sub-pixel resolution due to the Gaussian pattern of the laser beam) and a standard
 98 cross-correlation technique yielded similar estimates for the surface velocity.

99 2.3. Summary of experimental results

100 Figure 1 summarizes the experimental results. Figure 1a shows a time series of estimated
 101 wave steepness, and figure 1b shows the measured average surface velocity using TMV. The
 102 thick gray line in figure 1 plots At , where $A = 1 \text{ cm s}^{-1}$ showing that the surface current
 103 increases linearly in time. (The time axis for laboratory measurements is adjusted to meet
 104 this line, which constitutes a definition of “ $t = 0$ ”.) Following Veron & Melville (2001),
 105 figures 1a–b divide the development of the waves and currents into four stages:

106 (i) *Viscous acceleration*, $t = 0$ –16 s. In the first stage, viscous stress between the
 107 accelerating wind and water accelerates a shallow, laminar, viscous wind-drift layer.

108 (ii) *Wave-catalyzed “Langmuir” shear instability*, $t = 16$ –18 s. At $t \approx 16$ s, detectable
 109 capillary ripples appear. A wave-catalyzed shear instability — which obey the same dynamics
 110 as “Langmuir circulation”, which often refers to much larger scale motions in the ocean
 111 surface boundary layer Craik & Leibovich (1976) — immediately starts to develop and grow
 112 in the wind-drift layer.

113 (iii) *Self-sharpening*, $t = 18$ –20 s. When the shear instability reaches finite amplitude,
 114 nonlinear amplification due to perturbation self-advection sharpens the instability features
 115 into narrow jets and downwelling plumes.

116 (iv) *Langmuir turbulence*, $t > 20$ s. The self-sharpened circulations develop significant
 117 three-dimensional characteristics and transition to fully developed Langmuir turbulence.

118 3. A wave-averaged model for the transition to turbulence in wind-drift layers

119 The main purpose of this paper is to build a model for the four-stage evolution of the wind-drift
 120 layer, focusing on the dynamics after ripple inception.

121 3.1. Viscous acceleration

122 As the wind starts to accelerate, viscous stress across the air-water interface drives a laminar
 123 wind-drift current. The thick gray line in figure 1 indicates that the average surface velocity
 124 nearly obeys

125
$$U(z = 0, t) \equiv U_0(t) = A t, \quad (3.1)$$

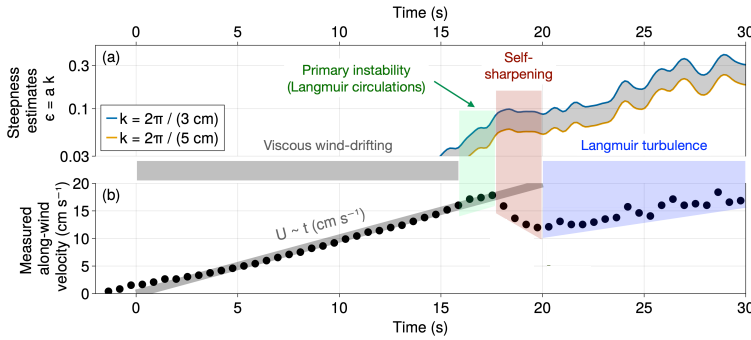


Figure 1: Summary of laboratory measurements: (a) an estimate of the steepness of the surface wave field that combines amplitude data with wavenumbers $k = 2\pi/3 \text{ cm}^{-1}$ and $k = 2\pi/5 \text{ cm}^{-1}$; (b) average surface along-wind velocity.

126 where $A \approx 1 \text{ cm s}^{-2}$. Veron & Melville (2001) point out that the viscous stress consistent
127 with linear surface current acceleration is

$$128 \quad \tau(t) = \alpha \sqrt{t} \hat{x} \quad (3.2)$$

129 where τ is the downwards kinematic stress across the air-water interface, \hat{x} is the along-wind
130 direction (\hat{y} and \hat{z} are the cross-wind and vertical directions), and $\alpha \approx 1.2 \times 10^{-5} \text{ m}^2 \text{ s}^{-5/2}$
131 produces $A = \alpha \sqrt{4/\pi\nu} \approx 1 \text{ cm s}^{-1}$ given the kinematic viscosity of water, $\nu = 1.05 \times$
132 $10^{-6} \text{ m}^2 \text{ s}^{-1}$. The laminar viscous solution beneath (3.2) is (Veron & Melville 2001)

$$133 \quad U(z, t) = U_0(t) \left[\left(1 + \delta^2 \right) \operatorname{erfc} \left(-\frac{\sqrt{2}}{2} \delta \right) + \delta \sqrt{\frac{2}{\pi}} \exp \left(-\frac{1}{2} \delta^2 \right) \right] \quad \text{where} \quad \delta \equiv \frac{z}{\sqrt{2\nu t}}. \quad (3.3)$$

134 Viscous acceleration continues until gravity-capillary ripples appear at the air-water interface
135 when $t \approx \tilde{t} \equiv 16$ seconds and thus $U_0(t) \approx \tilde{U}_0 \equiv 16 \text{ cm s}^{-1}$.

136 3.2. Instability of the wind-drift layer catalyzed by incipient capillary ripples

137 As soon as ripples appear on the water surface, a second, slower, non-propagating instability
138 begins to grow. Remarkably, this second instability is catalyzed by and therefore requires the
139 presence of capillary ripples: for example Veron & Melville (2001) show that instability and
140 turbulence are suppressed if ripple generation is suppressed by layering a surfactant on the
141 water surface.

142 Interestingly, ripple inception is not explained by linear theory (Young & Wolfe 2014).
143 We nevertheless assume that the ensuing dynamics are described by the weakly-nonlinear and
144 wave-averaged ‘‘Craik-Leibovich’’ momentum equation. This ansatz is supported by the data
145 in figure 1a, which plots an estimate of the wave steepness $\epsilon \equiv ak$, where a is the surface
146 wave amplitude (readily measured in the lab) and $k \approx 2\pi/3 \text{ cm}^{-1}$ – $2\pi/5 \text{ cm}^{-1}$ is the gravity-
147 capillary wavenumber for ripples with wavelengths between 3 and 5 cm (slightly larger than
148 the minimum gravity-capillary wavelength 1.7 cm). Apparently, by the time ripples reach
149 detectable amplitudes they have small slopes with $\epsilon < 0.1$.

150 The wave-averaged Craik-Leibovich equation (Craik & Leibovich 1976) formulated in
151 terms of the Lagrangian-mean momentum \mathbf{u}^L of the wind-drift layer is

$$152 \quad \mathbf{u}_t^L + (\mathbf{u}^L \cdot \nabla) \mathbf{u}^L - (\nabla \times \mathbf{u}^S) \times \mathbf{u}^L + \nabla p^E = \nu \Delta \mathbf{u}^L - \nu \Delta \mathbf{u}^S + \mathbf{u}_t^S, \quad (3.4)$$

153 where \mathbf{u}^S is the Stokes drift of the field of capillary ripples and p^E is the Eulerian-mean

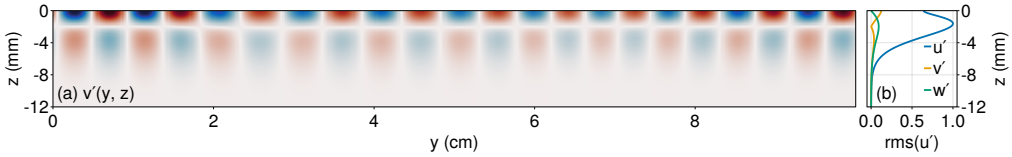


Figure 2: Structure of the most unstable eigenmode for wave steepness $\epsilon = 0.1$ in a 10×5 cm domain in (y, z) . (a) Structure of the cross-wind perturbation $v'(y, z)$ for wave steepness $\epsilon = 0.1$ in a 10×5 cm domain in (y, z) , (b) root-mean-square (y-averaged) perturbation profiles

154 pressure. The asymptotic derivation of the CL equation (3.4) requires $\epsilon \ll 1$. We require \mathbf{u}^L
155 to be divergence-free (Vanneste & Young 2022),

$$156 \quad \nabla \cdot \mathbf{u}^L = 0. \quad (3.5)$$

157 The Stokes drift associated with monochromatic capillary ripples propagating in the along-
158 wind direction $\hat{\mathbf{x}}$ is

$$159 \quad \mathbf{u}^S(z, t) = e^{2kz} \epsilon^2 c(k) \hat{\mathbf{x}}, \quad \text{where} \quad c(k) = \sqrt{\frac{g}{k} + \gamma k} \quad (3.6)$$

160 is the phase speed of gravity-capillary waves in deep water with gravitational acceleration
161 $g = 9.81 \text{ m s}^{-2}$ and surface tension $\gamma = 7.2 \times 10^{-5} \text{ m}^3 \text{ s}^{-2}$. In all cases considered here, the
162 Stokes drift (3.6) is minuscule compared to the mean current $\mathbf{u}^L \sim U$.

163 We invoke the power method (Constantinou 2015) to investigate the stability of the wind-
164 drift layer immediately following ripple generation. In our implementation of the power
165 method we extract the fastest growing mode perturbing the steady shear flow $\tilde{U}(z)$, such that

$$166 \quad \mathbf{u}^L(y, z, t) = \tilde{U}(z) \hat{\mathbf{x}} + \mathbf{u}(y, z, t), \quad (3.7)$$

167 where $\tilde{U}(z) \equiv U(z, \tilde{t})$ represents the wind-drift profile ‘frozen’ at $\tilde{t} = 16$ s and $\mathbf{u} = (u, v, w)$
168 is the perturbation velocity. Inserting (3.7) into (3.4)–(3.5), introducing a streamfunction ψ
169 with the convention $(v, w) = (-\psi_z, \psi_y)$, and neglecting terms that depend only on the mean
170 flow U or u^S yields the two-dimensional system

$$171 \quad u_t + J(\psi, u) + \Omega \psi_y = v \Delta u, \quad (3.8)$$

$$172 \quad \Delta \psi_t + J(\psi, \Delta \psi) + u_z^S u_y = v \Delta^2 \psi, \quad (3.9)$$

173 where $\Delta \psi = w_y - v_z$ is the x -component of the perturbation vorticity, $J(a, b) = a_y b_z - a_z b_y$
174 is the Jacobian operator, and $\Omega = \tilde{U}_z - u_z^S$ is the Eulerian-mean shear — or, as we prefer,
175 the mean, total cross-wind vorticity $\nabla \times (\tilde{U} \hat{\mathbf{x}} - \mathbf{u}^S) = \Omega \hat{\mathbf{y}}$. The power method isolates the
176 fastest growing linear modes of (3.8)–(3.9) by iterating over short integrations of the fully
177 nonlinear CL equations (3.4)–(3.5) from $t = \tilde{t}$ to $t = \tilde{t} + \Delta t$ and repeatedly downscaling \mathbf{u} via
178 (3.7) to ensure each integration has essentially linear dynamics.

179 Figure 2 shows the structure of the most unstable mode for $\epsilon = 0.1$. The mode is necessarily
180 sinusoidal in the horizontal because (3.8)–(3.9) is horizontally-uniform and has alternating
181 upwelling and downwelling regions, with a much larger streamwise component u' than cross-
182 stream and vertical components v' and w' . Figure 3 shows the results of a parameter sweep
183 from $\epsilon = 0.04$ to $\epsilon = 0.3$, illustrating how increasing ϵ leads to faster growth rates and
184 decreasing wavelengths of the fastest growing mode. We recover Veron & Melville (2001)’s
185 experimental result that shear instability does not occur without surface waves.

186 Note that the kinetic energy source for growing perturbations is the mean shear $\tilde{U}(z)$ and

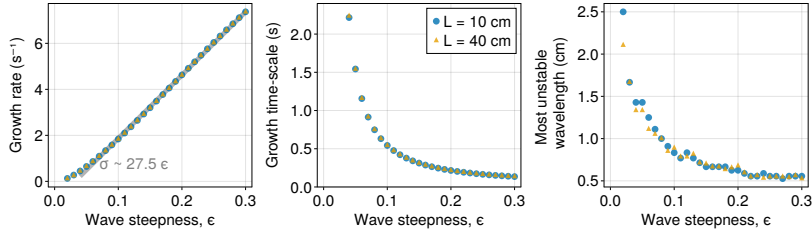


Figure 3: (a) Growth rate, (b) growth time-scale (inverse of the growth rate), and (c) wavelength of the most unstable mode of a wave-catalyzed instability of the wind-drift layer “frozen” at $\tilde{t} = 16$ seconds calculated using the power method (Constantinou 2015) in two domains 10 cm and 40 cm wide.

187 there is no energy exchange between perturbations and the surface wave field within the
 188 context of the wave-averaged equations (3.4)–(3.5). To see this, consider that (3.4)–(3.5)
 189 conserves total kinetic energy $\int \frac{1}{2} |\mathbf{u}^L|^2 dV$ when $\nu = 0$ and $\partial_t \mathbf{u}^S = 0$ (viscous stress is
 190 negligible). This is why we characterize the shear instability as “wave-catalyzed”: while the
 191 presence of waves is necessary for instability, and while the instability growth rate is strongly
 192 affected by wave amplitude, the kinetic energy of the growing perturbation is derived solely
 193 from the mean shear.

194 3.3. Self-sharpening circulations with jets and plumes

195 When the wave-catalyzed shear instability reaches finite amplitude, it begins to self-sharpen,
 196 producing narrow along-wind jets and downwelling plumes. The sharpening — but still two-
 197 dimensional — plumes then transport a measureable amount of mean momentum downwards
 198 before becoming unstable to three-dimensional perturbations and thereby transitioning to
 199 fully-developed turbulence. This nonlinear sharpening and depletion of the average near-
 200 surface momentum occurs between 17.5–20 seconds, as evidenced by the red shaded region
 201 in figure 1b.

202 To simulate the second wave-catalyzed instability through finite amplitude and toward
 203 transition to turbulence, we propose a simplified model based on the wave-averaged equations
 204 (3.4)–(3.5) with two main components representing (*i*) the capillary ripples and (*ii*) the
 205 initial condition at $\tilde{t} = 16$ seconds. We model the evolving capillary ripples as steady,
 206 monochromatic surface waves with wavenumber $k = 2\pi/3 \text{ cm}^{-1}$. We model the condition of
 207 the wave tank at $t = 16$ seconds with

$$208 \quad \mathbf{u}^L|_{t=\tilde{t}} = \tilde{U}(z)\hat{\mathbf{x}} + \mathbb{U}'\boldsymbol{\Xi}(x, y, z), \quad (3.10)$$

209 where \mathbb{U}' is an initial noise amplitude and $\boldsymbol{\Xi}$ is a vector whose components are normally-
 210 distributed random numbers with zero mean and unit variance.

211 Through experimentation, we find that the instability and transition to turbulence are only
 212 weakly sensitive to the wavenumber k . The tuning parameters of our model are therefore
 213 (*i*) the amplitude of the initial perturbation \mathbb{U}' , and (*ii*) the wave steepness ϵ . We discuss
 214 possible interpretations for \mathbb{U}' in section 4.

215 We also simulate the evolution of dye concentration θ via

$$216 \quad \partial_t \theta + \mathbf{u}^L \cdot \nabla \theta = \kappa \Delta \theta, \quad (3.11)$$

217 with molecular diffusivity $\kappa = 10^{-7} \text{ m}^2 \text{ s}^{-1}$, the smallest we can reasonably afford computa-
 218 tionally. (The correspondance between θ and rhodamine is imperfect because the molecular
 219 diffusivity of rhodamine is $\kappa = 10^{-9} \text{ m}^2 \text{ s}^{-1}$.) We initialize θ with a δ -function at the surface.
 220 We integrate (3.4)–(3.5) and (3.11) given (3.6) using Oceananigans (see Ramadhan *et al.*

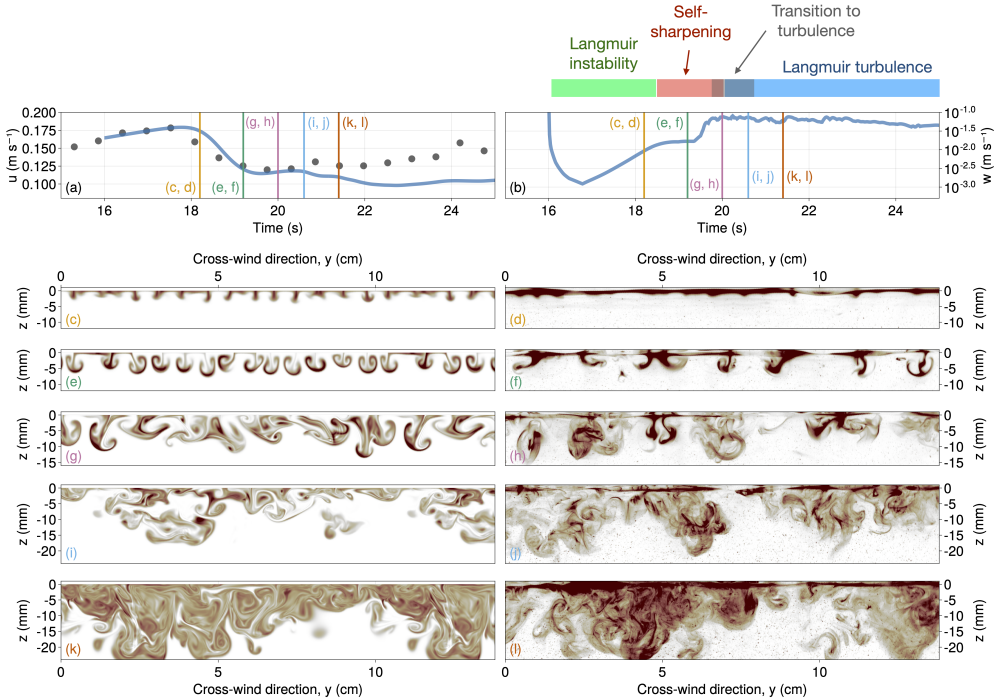


Figure 4: (a) Maximum horizontal velocity u . The grey dots are from the laboratory experiments while the blue line shows the numerical experiments. (b) Vertical velocity. (c-l) Evolution of the wind-drift layer after the emergence of capillary ripples.

2020 and Wagner *et al.* 2021) with a second-order staggered finite volume method on a single
222 A100 GPU in a $10 \times 10 \times 5$ cm domain in (x, y, z) with 0.13 mm regular spacing in x, y
223 and variable spacing in z with $\min(\Delta z) \approx 0.26$ mm, corresponding to $768 \times 768 \times 512$ finite
224 volume cells.

The results are visualized in figure 4. Figure 4a compares the average surface velocity diagnosed from the simulation with the laboratory measurements presented in figure 1b. Figure 4b plots the maximum absolute vertical velocity, $\max |w^L|$. Figures 4c–l compare the simulated dye concentration on (y, z) slices with LIF measurements of rhodamine from the laboratory experiment, showing the particularly good qualitative agreement between simulated and measured dye features. Visualizations are shown at $t = 18.1, 19.3, 20.0, 20.7$, and 21.7 seconds. At $t = 18.1$ s (figures 4c and d), the sharpened plumes have only just started advect appreciable amounts of dye. At $t = 19.3$ seconds (figures 4 e and f), the plumes are beginning to roll up into two-dimensional mushroom-like structures. (Note the small, unexplained discrepancy between simulated and measured average surface velocities around $18.1 < t < 19.3$.) At $t = 20.0$ seconds and $t = 20.7$ (figures 4g, h, i, and j) three-dimensionalization and transition to turbulence are underway. At $t = 21.7$ both the simulated and measured dye concentrations appear to be mixed by three-dimensional turbulence.

Figure 5 illustrates the sensitivity of the wave-averaged model to amplitude of the specified surface ripples and to the amplitude of the random initial perturbation. Figures 5a and b plot the surface-averaged along-wind velocity u and maximum vertical velocity w for two wave amplitudes $\epsilon = 0.1$ and $\epsilon = 0.11$, and for two initial perturbation amplitudes $\mathbb{U}' = 5 \text{ cm s}^{-1}$ and $\mathbb{U}' = 10 \text{ cm s}^{-1}$. The dependence of the maximum vertical velocity is the most evocative: doubling the initial perturbation shortens the self-sharpening phase (in

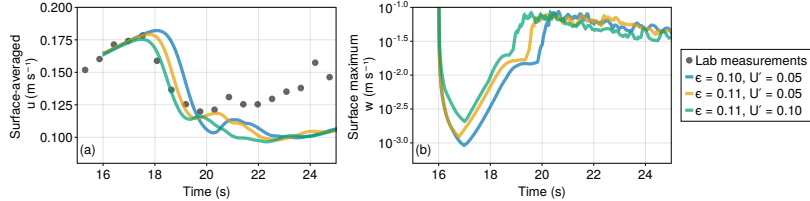


Figure 5: Sensitivity of (a) surface-averaged along-wind velocity u and (b) maximum vertical velocity to the specification of the surface wave field and initial perturbations.

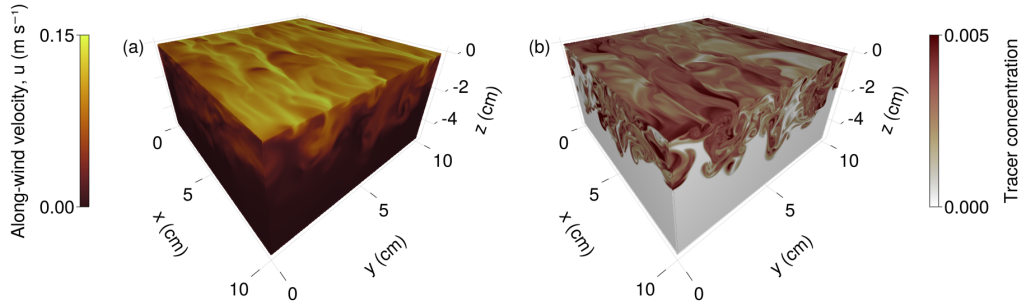


Figure 6: (a) Simulated x -momentum and (b) dye concentration at $t = 23.4$ seconds, showing the streaks and jets that characterize Langmuir turbulence.

which the maximum vertical velocity in figure 5b flattens before increasing sharply during the transition to turbulence) by a factor of five. Of the three cases plotted in figure 5, only $\epsilon = 0.11$ and $U' = 5 \text{ cm s}^{-1}$ yield the satisfying agreement depicted in figure 4.

247

3.4. Langmuir turbulence

248 Following three-dimensionalization, momentum and dye are rapidly mixed to depth. Figure 6
249 visualizes (a) the x -momentum and (b) dye concentration at $t = 23.4$ seconds, showing how
250 the flow is organized into narrow along-wind streaks and broader downwelling regions —
251 classic characteristics of Langmuir turbulence (Sullivan & McWilliams 2010).

252 In figure 7, we compare the rate which dye is mixed to depth in the simulations versus
253 measured by LIF in the lab. Figure 7a shows the simulated horizontally-averaged tracer
254 concentration in the depth-time (z, t) plane, while figure 7b shows a corresponding laboratory
255 measurements extracted from LIF measurements in the (y, z)-plane. In figures 7a and b, a
256 light blue line shows the height $z_{99}(t)$ defined as the level above which 99% of the *simulated*
257 tracer concentration resides,

$$258 \int_{z_{99}(t)}^0 \theta dz = 0.99 \int_{-H}^0 \theta dz. \quad (3.12)$$

259 Using $z_{99}(t)$ to compare the tracer mixing rates exhibited in figures 7a and b, we conclude that
260 the simulations provided a qualitatively accurate prediction of dye mixing rates. If anything,
261 the simulation *overpredicts* the dye mixing rate — but the data probably does not warrant
262 more than broad qualitative conclusions.

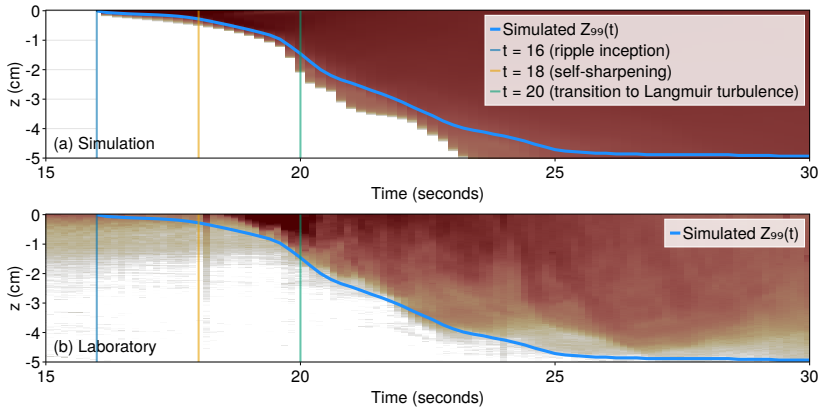


Figure 7: Visualization of mixing rates during measured and simulated wave-catalyzed instability via depth-time (z, t) diagrams of horizontally-averaged in (a) simulations and (b) LIF-measurements. The blue lines denotes the depth above which 99% of the simulated dye resides; (b) suggests that the simulations overpredict dye mixing rates.

263 4. Discussion

264 This paper describes a wave-averaged model for the evolution of wind-drift layers following
 265 the inception of capillary ripples. The wave-averaged model predicts that, following ripple
 266 incipition, the wind-drift layer is immediately susceptible to the growth of a second, slower,
 267 “wave-catalyzed” instability. Wave-averaged simulations show that the evolution of the wave-
 268 catalyzed instability from initial growth through transition to turbulence is sensitive not only
 269 to the amplitude of the surface ripples, but also to the amplitude of the perturbations that
 270 seed the growth of the second-instability and also destabilize the jets and plumes during the
 271 transition to turbulence.

272 We model the seeding and destabilizing perturbations modeled as random velocity
 273 fluctuations imposed at the time of ripple inception. However, in wind-drift layers in the
 274 laboratory or natural world, perturbations may be continuously introduced both by turbulent
 275 pressure fluctuations in the air and, perhaps, by inhomogeneities in the ripple field (see
 276 figures 3 and 15 in Veron & Melville 2001). The natural prevalence of the striking coherent
 277 structures observed in the laboratory and visualized in figure 4 is therefore uncertain.

278 One of the original goals of this work was to probe the potential weaknesses of the wave-
 279 averaged Craik-Leibovich (CL) equation, which are widely used for process studies and
 280 parameterization of ocean surface boundary layer turbulence (Sullivan & McWilliams 2010).
 281 In particular, the derivation of the CL equation requires the restrictive assumptions that (i)
 282 the surface wave field is nearly linear; and (ii) the timescale of the turbulence is much longer
 283 than the time scale of the waves. But despite qualitative success, firm conclusions about CL
 284 validity prove elusive due to the strong sensitivity of our results to ripple amplitude — which
 285 is evolving and two-dimensional in the laboratory experiments rather than uniform and steady,
 286 as in our model. This sensitivity, together with Veron & Melville (2001)’s observations that
 287 the ripple field is refracted and organized by turbulence in the wind-drift layer, suggests that
 288 two-way wave-turbulence coupling is important and should be described in a “predictive”
 289 theory for turbulent boundary layers affected by surface waves. Further progress requires
 290 not just theoretical advances to couple wave evolution with the CL equations, but also
 291 experiments that obtain more precise two-dimensional measurements of the evolution of the
 292 capillary ripples.

293 *Acknowledgements.* GLW's work is supported by the generosity of Eric and Wendy Schmidt
 294 by recommendation of the Schmidt Futures program and by the National Science Foundation
 295 grant AGS-1835576. We acknowledge stimulating discussions with Bill Young and Navid
 296 Constantinou.

REFERENCES

- 297 BUCKLEY, MARC P & VERON, FABRICE 2017 Airflow measurements at a wavy air–water interface using piv
 298 and lif. *Experiments in Fluids* **58** (11), 161.
- 299 CONSTANTINOU, NAVID C 2015 Formation of large-scale structures by turbulence in rotating planets. *arXiv*
 300 *preprint arXiv:1503.07644*.
- 301 CRAIK, ALEX DD & LEIBOVICH, SIDNEY 1976 A rational model for Langmuir circulations. *Journal of Fluid*
 302 *Mechanics* **73** (3), 401–426.
- 303 D'ASARO, ERIC A., THOMSON, J., SHCHERBINA, AY, HARCOURT, RR, CRONIN, MF, HEMER, MA & FOX-
 304 KEMPER, B 2014 Quantifying upper ocean turbulence driven by surface waves. *Geophysical Research*
 305 *Letters* **41** (1), 102–107.
- 306 HANDLER, RA, SMITH, GB & LEIGHTON, RI 2001 The thermal structure of an air–water interface at low
 307 wind speeds. *Tellus A* **53** (2), 233–244.
- 308 HARCOURT, RAMSEY R 2015 An improved second-moment closure model of langmuir turbulence. *Journal*
 309 *of Physical Oceanography* **45** (1), 84–103.
- 310 JESSUP, AT, ZAPPA, CHRISTOPHER J & YEH, HARRY 1997 Defining and quantifying microscale wave breaking
 311 with infrared imagery. *Journal of Geophysical Research: Oceans* **102** (C10), 23145–23153.
- 312 MELVILLE, W KENDALL, SHEAR, ROBERT & VERON, FABRICE 1998 Laboratory measurements of the
 313 generation and evolution of Langmuir circulations. *Journal of Fluid Mechanics* **364**, 31–58.
- 314 RAMADHAN, ALI, WAGNER, GREGORY, HILL, CHRIS, CAMPIN, JEAN-MICHEL, CHURAVY, VALENTIN,
 315 BESARD, TIM, SOUZA, ANDRE, EDELMAN, ALAN, FERRARI, RAFFAELE & MARSHALL, JOHN 2020
 316 Oceananigans. jl: Fast and friendly geophysical fluid dynamics on gpus. *Journal of Open Source*
 317 *Software* **5** (53).
- 318 REICHL, BRANDON G & LI, QING 2019 A parameterization with a constrained potential energy conversion
 319 rate of vertical mixing due to langmuir turbulence. *Journal of Physical Oceanography* **49** (11),
 320 2935–2959.
- 321 SULLIVAN, PETER P & McWILLIAMS, JAMES C 2010 Dynamics of winds and currents coupled to surface
 322 waves. *Annual Review of Fluid Mechanics* **42**, 19–42.
- 323 SUTHERLAND, PETER & MELVILLE, W KENDALL 2013 Field measurements and scaling of ocean surface
 324 wave-breaking statistics. *Geophysical Research Letters* **40** (12), 3074–3079.
- 325 THORPE, SA 2004 Langmuir circulation. *Annu. Rev. Fluid Mech.* **36**, 55–79.
- 326 VANNESTE, JACQUES & YOUNG, WILLIAM R 2022 Stokes drift and its discontents. *Philosophical Transactions*
 327 *of the Royal Society A* **380** (2225), 20210032.
- 328 VERON, FABRICE & MELVILLE, W KENDALL 1999 Pulse-to-pulse coherent doppler measurements of waves
 329 and turbulence. *Journal of Atmospheric and Oceanic Technology* **16** (11), 1580–1597.
- 330 VERON, FABRICE & MELVILLE, W KENDALL 2001 Experiments on the stability and transition of wind-driven
 331 water surfaces. *Journal of Fluid Mechanics* **446**, 25–65.
- 332 VERON, FABRICE, MELVILLE, W KENDALL & LENAIN, LUC 2008 Wave-coherent air–sea heat flux. *Journal*
 333 *of physical oceanography* **38** (4), 788–802.
- 334 WAGNER, GREGORY L, CHINI, GREGORY P, RAMADHAN, ALI, GALLET, BASILE & FERRARI, RAFFAELE 2021
 335 Near-inertial waves and turbulence driven by the growth of swell. *Journal of Physical Oceanography*
 336 **51** (5), 1337–1351.
- 337 YOUNG, WR & WOLFE, CL 2014 Generation of surface waves by shear-flow instability. *Journal of fluid*
 338 *mechanics* **739**, 276–307.
- 339 ZAPPA, C. J., ASHER, W. E. & JESSUP, A. T. 2001 Microscale wave breaking and air-water gas transfer.
 340 *Journal of Geophysical Research: Oceans* **106** (C5), 9385–9391.